Controlling strong-field fragmentation of H_2^+ by temporal effects with few-cycle laser pulses

J. McKenna, F. Anis, A. M. Sayler, B. Gaire, Nora G. Johnson, E. Parke, K. D. Carnes, B. D. Esry, and I. Ben-Itzhak

J.R. Macdonald Laboratory, Department of Physics, Kansas State University, Manhattan, Kansas 66506, USA

(Received 24 November 2011; published 13 February 2012)

In a joint experimental and theoretical endeavor, we explore the laser-induced dissociation and ionization dynamics of H_2^+ beams using sub-10-fs, 800 nm laser pulses. Our theory predicts considerable control over the branching ratio of two-photon and three-photon above-threshold dissociation (ATD) by gating the dissociation pathway on a few-femtosecond timescale. We are able to experimentally demonstrate this control. Moreover, our theory also shows the importance of the highly excited H($2l$) states of H_2^+ that contribute to ATD structure in dissociation. As is the case for dissociation, we find that ionization is also sensitive to the effective laser interaction time.

DOI: 10.1103/PhysRevA.85.023405 PACS number(s): 33.80.Wz, 42.50.Hz

I. INTRODUCTION

Staggering progress in understanding the dynamics of small molecules in intense ultrashort laser fields has been made over the past 20 years (see, e.g., Refs. [1,2] and references therein). The progress has benefited enormously from the rapid development of modern laser technology. One of the earliest and still-active goals of laser-molecule research is the exciting prospect of controlling the products of chemical reactions [3]. As a proof-of-principle, the simplest molecule, H_2^+, is often the target of choice to demonstrate new techniques. To this end, pioneering experimental and theoretical demonstrations of control of the dissociation of H_2^+ (or HD^+ or D_2^+) have been achieved, for example, by using pump-probe delay [4–6], two-color fields [7–13], and the carrier-envelope phase (CEP) of the laser pulse [14–21].

We recently demonstrated an alternative method of influencing H_2^+ dissociation [22] that bears analogies to early theoretical work on Na_2^+ [23]. The objective of our H_2^+ experiment was to enhance above-threshold dissociation (ATD) by three or more photons, which we termed "high-order ATD" for convenience. The scheme used is illustrated in Fig. 1 and depends wholly on the duration of the laser interaction with respect to the timescale of dissociation.

Ground state ($1s\sigma_g$) H_2^+ will start to dissociate on the excited $2p\sigma_u$ state from an internuclear distance R of about 3.3 a.u. following the absorption of three photons at 800 nm. If the laser pulse is long (>10 fs), the dissociative H_2^+ nuclear wave packet will be strongly transferred back to the $1s\sigma_g$ state as it passes through the one-photon resonance ($R = 4.8$ a.u.), accompanied by the emission of one photon. This results in *net* two-photon (2ω) dissociation and is typically the strongest ATD mechanism observed both in experiments and theory (see, e.g., Refs. [24,25]). On the other hand, if the laser pulse is sufficiently short (∼5 fs) such that the intensity is low when the wave packet passes through the one-photon resonance, then the wave packet is only weakly transferred back to the $1s\sigma_g$ state. As a result, a sizable fraction of the population remains on the $2p\sigma_u$ state and dissociates via the direct three-photon (3ω) pathway. The difference in dissociation energy between two-photon and three-photon ATD is roughly the energy of one photon and, to a fair extent, may be distinguished by kinetic energy release (KER).

The important factor in this scheme is the timescale for the nuclear wave packet to travel from the three-photon resonance (R_3) to the one-photon resonance (R_1). Classically, for an H_2^+ wave packet starting from rest on the $2p\sigma_u$ potential at $R_3 = 3.3$ a.u., it takes 4.7 fs to reach the next resonance at $R_1 = 4.8$ a.u. For D_2^+, this time is increased to 6.7 fs because the wave packet is slower by a factor of $\sqrt{2}$ due to the larger nuclear mass. Therefore, for the same short pulse one can expect more high-order ATD from D_2^+ than from H_2^+. Based on reduced mass, it is expected that HD^+ will be in between H_2^+ and D_2^+, although we note that, due to its heteronuclear character, HD^+ has the potential to produce, for example, permanent dipole transition features—those, however, are expected to be very small [26].

In addition to ATD from the lowest two electronic states of H_2^+ corresponding to the H($1s$) manifold, our theoretical calculations also show a surprisingly large contribution to ATD from the H($2l$) manifold of excited states. The H($2l$) states, shown in Fig. 1, lie more than 10 eV above the H($1l$) states and, for this reason, are omitted from most other theoretical calculations. However, our calculations at $\sim 10^{14}$ W/cm^2 show that, for certain KER values, the contributions to ATD from the H($2l$) states can outweigh ATD from the H($1l$) states.

In this paper we extend our earlier study [22] to explore in more detail the intensity, pulse length, and mass dependence of the ATD processes, both theoretically and experimentally. This knowledge is vital because it gives further insight into the dynamics of H_2^+ in few-cycle pulses. This is important considering the present focus on ultrashort laser work. In addition, we show the experimental results of ionization of H_2^+ beams using few-cycle pulses. On the few-cycle timescale, ionization, like dissociation, displays a strong pulse-length dependence.

The target we use is a beam of H_2^+ ions formed via electron-impact ionization of H_2 in an electron cyclotron resonance (ECR) ion source. This is different from the more conventional method that creates H_2^+ by ionizing a neutral H_2 gas target with the same laser pulse that is used for the subsequent fragmentation (see, e.g., Ref. [27]). Although the ion-beam method [28–39] makes the experiments considerably more difficult to perform due to much lower target densities (e.g., for conditions used in this paper, the

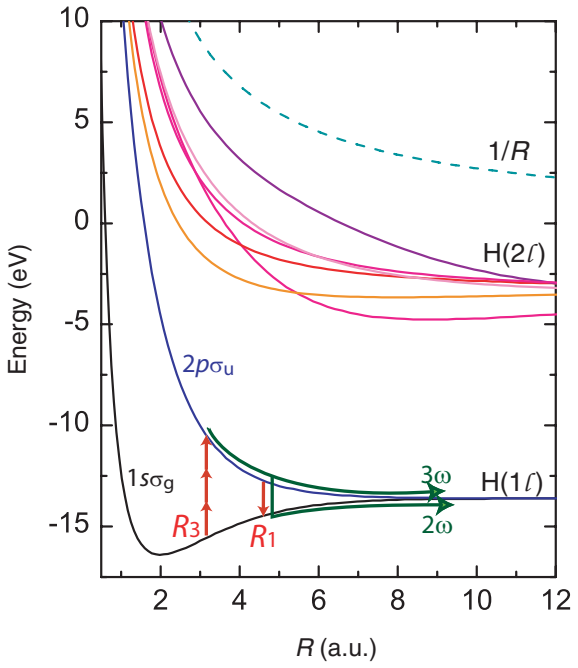

FIG. 1. (Color online) Potential energy curves of H_2^+ displaying the H($1l$) states leading to $H^+ + H(1s)$ and the H($2l$) states leading to $H^+ + H(2l)$. The ionization curve, $1/R$, leading to $H^+ + H^+$ is also displayed. The vertical arrows labeled R_1 and R_3 denote the one-photon and three-photon resonance positions, respectively.

ion-beam target density is lower by more than four orders of magnitude than a gas target at 10^{-7} Torr), H_2^+ produced in this way has at least three different properties that are important for the high-order ATD control scheme introduced above.

First, H_2^+ will begin to dissociate at much lower intensity because the intensity is not required to be above the ionization threshold of H_2. This allows excitation to the $2p\sigma_u$ state by a three-photon absorption to occur immediately at its onset intensity, thereby triggering the dissociation process early in the pulse. Second, there is no initially ionized electron (born from H_2) that can be driven by the laser field. This ensures that electron-recollision [40,41] dissociation of H_2^+ cannot occur, which may otherwise obscure the observation of high-order ATD since the KER of these two processes is known to overlap [42]. Third, the ion-beam technique allows detection of neutral fragments, as well as ionic ones, thereby enabling a coincidence between dissociation fragments and separating them from ionization [30]. This is important because our results show that the high-order ATD and the ionization spectra overlap in KER.

II. TECHNICAL DETAILS

A. Theory

1. Choice of representation

We solved the time-dependent Schrödinger equation for H_2^+ in the intense laser field using the dipole approximation in the length gauge. The Schrödinger equation thus reads (atomic units are used throughout unless otherwise stated)

$$i\frac{\partial}{\partial t}\Psi(\mathbf{r},\mathbf{R},t) = \left(-\frac{1}{2\mu}\nabla_R^2 - \frac{1}{2}\nabla_r^2 - \frac{1}{r_A} - \frac{1}{r_B} + \frac{1}{R} - \boldsymbol{\mathcal{E}}(t)\cdot\mathbf{d}\right)\Psi(\mathbf{r},\mathbf{R},t), \quad (1)$$

where $\mu = m/2$ (for homonuclear molecules), m is the nuclear mass, R is the internuclear distance, r_A and r_B are the distances of the electron from the two nuclei, and $\mathbf{d}$ is the dipole operator. In all the calculations, we used a linearly polarized field with a Gaussian envelope [43],

$$\boldsymbol{\mathcal{E}}(t) = \boldsymbol{\mathcal{E}}_0 e^{-t^2/\tau^2}\cos(\omega t + \varphi). \quad (2)$$

The laser polarization was fixed along the laboratory-frame $\hat{z}$ axis, the laser frequency ω was 0.058 a.u. corresponding to 785 nm, and the carrier-envelope phase φ will be discussed below.

We solved Eq. (1) using the Born-Oppenheimer representation. The total wave function $\Psi(\mathbf{r},\mathbf{R},t)$ is then

$$\Psi(\mathbf{r},\mathbf{R},t) = \sum_\alpha F_\alpha(R,t)\Phi_\alpha(R;\mathbf{r},\theta,\phi). \quad (3)$$

Here, $\alpha = \{J,M,\Pi,n,\Lambda,\sigma_z\}$ labels each basis state with the total orbital angular momentum J and its laboratory frame z projection M, total parity Π, principal quantum number in the separated-atom limit n, projection of the electron orbital angular momentum along the internuclear axis in the body-fixed frame Λ, and reflection symmetry through $z = 0$ in the body-fixed frame σ_z. In this notation, $\sigma_z(-1)^\Lambda = \pm 1$ corresponds to the usual "gerade" and "ungerade" symmetries, respectively.

We include the spherical angles θ and ϕ of the internuclear axis with respect to the laboratory frame with the electronic degrees of freedom in the adiabatic basis functions $\Phi_\alpha(R;\mathbf{r},\theta,\phi)$.

So, neglecting all the non-Born-Oppenheimer coupling terms and the Coriolis coupling, we can write

$$\Phi_\alpha(R;\mathbf{r},\theta,\phi) = \phi_{n\sigma_z\Lambda}(R;\xi,\eta)\Omega^{J\pi}_{M\Lambda}(\theta,\phi,\chi). \quad (4)$$

The electronic states $\phi_{n\sigma_z\Lambda}(R;\xi,\eta)$ were calculated using the method described in Ref. [44]. The body-frame electronic azimuthal coordinate χ has been incorporated into the angular momentum function $\Omega^{J\pi}_{M\Lambda}$, which is defined in terms of Wigner D functions as

$$\Omega^{J\pi}_{M\Lambda}(\theta,\phi,\chi) = \sqrt{\frac{2J+1}{8\pi^2}}\frac{1}{\sqrt{[b]2(1+\delta_{\Lambda 0})}}\left[D^J_{-M-\Lambda}(\phi,\theta,\chi) + \pi(-1)^{J+\Lambda}D^J_{-M\Lambda}(\phi,\theta,\chi)\right]. \quad (5)$$

Substituting Eq. (3) into Eq. (1) and projecting onto $\langle\Phi_\alpha|$ yields a set of coupled, one-dimensional, time-dependent differential equations for the nuclear wave functions $F_\alpha(R;t)$ (see Ref. [45] for details).

2. Extracting observables

To compare with the experiment, we calculate the KER-$\cos\theta_K$ distribution of the dissociating fragments. We do so by projecting the wave function at the end of the pulse onto properly symmetrized scattering states superposed to

asymptotically give a plane wave with momentum **K** (**K** is the relative momentum vector from H to p, making an angle θ_K with the polarization direction). Some of the less-appreciated points of this procedure are discussed in Refs. [46–49].

Restricting the expansion in Eq. (3) to include only $1s\sigma_g$ and $2p\sigma_u$ gives explicitly for the KER-cos θ_K distribution

$$\frac{\partial^2 P}{\partial E \partial \theta_K} = 2\pi \left| \sum_{J \text{ even}} C_{Jg}(E) Y_{JM}(\theta_K, 0) + \sum_{J \text{ odd}} C_{Ju}(E) Y_{JM}(\theta_K, 0) \right|^2 . \quad (6)$$

Here, $E = K^2/(2\mu)$ is the KER, $Y_{JM}(\hat{K})$ are spherical harmonics, and

$$C_{Jg(u)}(E) = (-i)^J e^{-i\delta_{Jg(u)}(E)} \langle EJg(u) | F_{Jg(u)}(t_f) \rangle, \quad (7)$$

with $|F_{Jg(u)}(t_f)\rangle$ being the nuclear radial functions at the final time t_f. Finally, $|EJg(u)\rangle$ are the energy-normalized radial scattering states, and $\delta_{Jg(u)}(E)$ are the scattering phase shifts.

As expected [50], Eq. (6) shows that the momentum distribution is a coherent sum of the $1s\sigma_g$ and $2p\sigma_u$ channels. Such a superposition can, in principle, produce an asymmetric distribution about $\theta_K = \frac{\pi}{2}$—especially given the shorter pulses used here. Any such asymmetry will vary with the carrier-envelope phase φ in Eq. (2) [14,16,21]. In the experiments, however, φ was not controlled, so we assume it had a uniform distribution between 0 and 2π. The calculated momentum distributions must therefore be averaged over φ. Using the general theory of carrier-envelope-phase effects that we developed in Ref. [18], this average can be done analytically to a good approximation (better than 1% error for our laser parameters). The analysis in Ref. [18] shows that the φ-averaged momentum distribution can be simply obtained from a calculation at a single φ using

$$\left\langle \frac{\partial^2 P}{\partial E \partial \theta_K} \right\rangle = 2\pi \left| \sum_{J \text{ even}} C_{Jg}(E) Y_{JM}(\theta_K, 0) \right|^2 + 2\pi \left| \sum_{J \text{ odd}} C_{Ju}(E) Y_{JM}(\theta_K, 0) \right|^2 . \quad (8)$$

In our case, we set $\varphi = 0$.

The KER distribution for the lowest two channels can simply written be as

$$\left\langle \frac{dP}{dE} \right\rangle = \int \left\langle \frac{\partial^2 P}{\partial E \partial \theta_K} \right\rangle \sin\theta_K d\theta_K = \sum_{J \text{ even}} |C_{Jg}(E)|^2 + \sum_{J \text{ odd}} |C_{Ju}(E)|^2 . \quad (9)$$

For simplicity, in the remainder of the paper, we drop the $\langle\cdot\rangle$ notation when referring to CEP-averaged observables and denote θ_K as θ [not to be confused with the spherical angle in Eq. (3)]. Extending this idea to the higher electronic states, we have calculated the KER distribution of these channels by projecting their time-dependent radial functions onto the corresponding energy-normalized scattering states. But, since there are degenerate σ_g and σ_u states within the $n = 2$ manifold, the incoherent sum in Eq. (9) is only an approximation to the physical KER distribution. By analyzing individual molecular channels, however, we found that any coherence present does not affect the qualitative behavior of the KER distributions or our conclusions. An incoherent sum over all the molecular channels as in Eq. (9) has thus been used for the total KER distribution (see note [51]).

The KER-cos θ analysis of the higher excited channels of H_2^+ is similarly complicated by the degeneracy of the excited H states and all that this implies. Since the total population of the H($2l$) manifold is less than 5% for all calculations, however, our theoretical KER-cos θ distributions include only the $1s\sigma_g$ and $2p\sigma_u$ channels. We emphasize that the time-dependent calculation included *all* channels as did the KER distributions—only the KER-cos θ analysis excluded the higher-excited channels. Overall, the omission of higher channels from the KER-cos θ distributions leads to only a small deviation from the true distributions. Nevertheless, as we will show, the omission can present a larger discrepancy in a localized region—for example, at KER values where dissociation on the H($2l$) manifold is dominant. In such cases, the KER distributions are more insightful because these do include higher channels.

3. *Numerical analysis*

We solved the resulting set of equations for $F_\alpha(R;t)$ numerically by approximating the radial kinetic energy operator with a generalized three-point-difference scheme [52,53]. The time evolution combined split operator techniques with a Crank-Nicolson-like propagator. We have implemented similar propagation schemes previously [32,45,52]. In all cases, the theoretical results were obtained by separately propagating all the $J = 0$ bound vibrational states of the $1s\sigma_g$ channel of H_2^+ (D_2^+), then incoherently averaging their observables over a Franck-Condon vibrational distribution [32]. We use $J = 0$ for the initial rotational states because the precise experimental J distribution is unknown while an estimate of the Boltzmann distribution shows that the population is concentrated around low J values. Tests indicate that the choice of initial J state does not affect any of our conclusions.

We took advantage of the generalized difference scheme's flexibility to use a nonuniform spatial grid based on the local wavelength determined from the maximum expected total energy. Specifically, in an 80 a.u. box, we used the Wentzel-Kramers-Brillouin (WKB) approximation to calculate the R-dependent phase at the maximum energy. Then, we placed a given number of grid points uniformly in each 2π (one de Broglie wavelength) interval of this phase. In a multichannel problem, the shortest wavelength is determined by the lowest accessible channel—$1s\sigma_g$ for H_2^+. This grid distribution is different from the one used in our previous studies [22,45], and we found it to give convergence with fewer points.

For the results presented here, we used 20 points per wavelength, based on a highest KER of 4.08 eV (0.15 a.u.). For the time propagation, we used a time step of 0.5 a.u. with the initial time determined from requiring the intensity to be 10^8 W/cm^2 and the final time determined from requiring the intensity to be 10^6 W/cm^2. In our calculations, the maximum value of J included in the expansion of Ψ, Eq. (3), was increased dynamically using a tolerance of 10^{-7} at every

time step (see Ref. [45] for details). With this prescription, 48 partial waves were required to do the calculations for 10 fs pulses at a peak intensity of 10^{14} W/cm^2. Convergence with respect to all of these parameters was verified and found to give the Franck-Condon-averaged total dissociation probability converged to at least three digits. The Franck-Condon-averaged KER distributions converged to no worse than 1.22%. The total dissociation probability for each initial vibrational state is converged to 0.33% for $v = 0$–17 of H_2^+, but only to 1.9% and 3.9% for $v = 18$ and 19, respectively. It should be noted that these larger errors do not translate into larger errors in the Franck-Condon–averaged observables since their contribution in this average is negligible.

B. Experimental setup

Some of the experimental details have been introduced previously [30,32]. The laser pulses in our experiments were generated using the Kansas Light Source (KLS) laser system [54]. This is a Kerr-lens mode-locked Ti:sapphire laser (central wavelength 800 nm) with a multipass amplifier (14 passes). It consists of a grating-based stretcher and compressor. After pulse compression, the system outputs ~30 fs Fourier-transform–limited pulses with an energy of 2.0 mJ at 1 kHz repetition rate. To further temporally compress the pulses, they were focused into a hollow-core fiber of diameter 400 μm and interaction length 1 m using an $f = 1$ m spherical mirror. The large core diameter facilitated the high input pulse energy. During propagation in the neon-filled fiber the pulses underwent spectral broadening from about 30 nm bandwidth (full-width at half maximum) to more than 200 nm due to self-phase modulation. Upon exiting the fiber the pulses were collimated using an $f = 1$ m spherical mirror and then compressed by reflection off chirped mirrors. These mirrors also compensated for additional dispersion acquired during propagation to our ion-beam interaction chamber. The pulse energy at this stage was 1.0 mJ and the optimum pulse duration was measured to be 7 fs by frequency-resolved optical gating (FROG), close to the Fourier-transform limit. For some measurements the pulses were intentionally lengthened to 10 fs by reducing the gas pressure in the fiber and hence the amount of spectral broadening.

From the fiber, the pulses were transported to the ion-beam apparatus under vacuum to maintain good beam quality. A 90° off-axis parabolic mirror ($f = 203$ mm) mounted to a multiple axis translation stage focused the pulses into our ion beam apparatus and onto the target. The laser focus was characterized by performing a z scan and imaging the focus onto a CCD camera. The focal beam waist diameter and Rayleigh range were measured to be 17 and 900 μm, respectively.

The ion-beam apparatus consisted of an ultrahigh vacuum (UHV) system with a base pressure of 2×10^{-10} Torr in the interaction chamber. The molecular ions were initially formed in an electron-cyclotron resonance (ECR) ion source. This operates by electron-impact ionization of H_2 to produce H_2^+. To a good approximation, the H_2^+ molecules are populated in a Franck-Condon distribution [55,56] of vibrational states [see Fig. 8(d)]. The H_2^+ ions were then extracted and accelerated to 9.0 keV. A sequence of electrostatic lenses (i.e., einzel

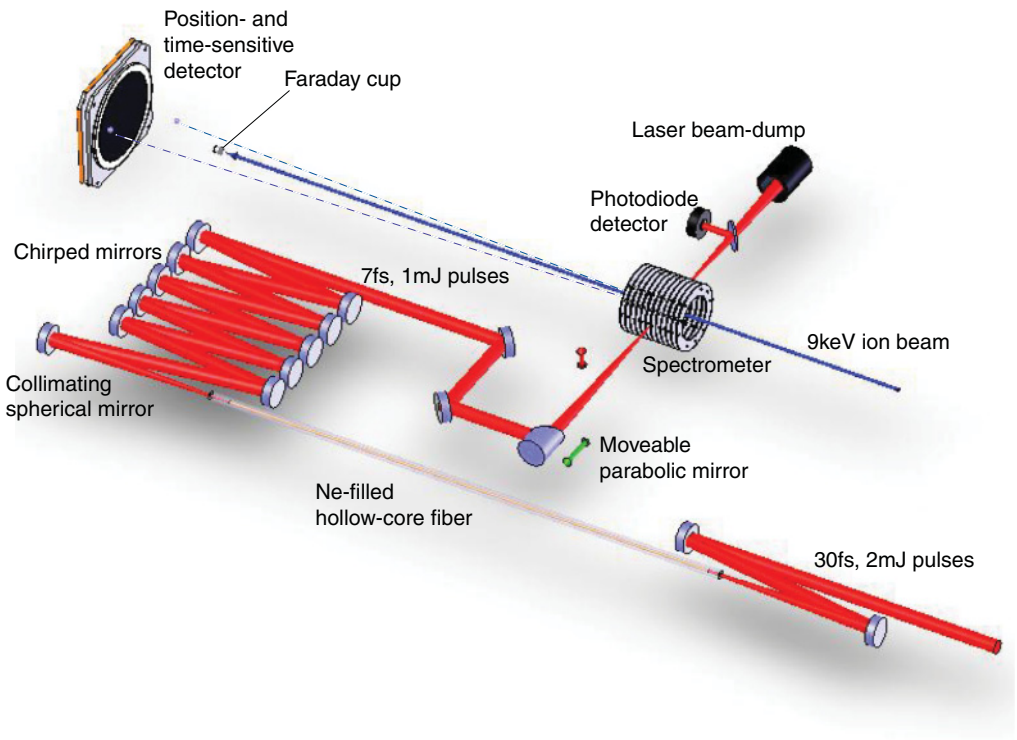

FIG. 2. (Color online) Schematic of experimental setup. Pulses from a hollow-core fiber and chirped-mirror arrangement are focused onto the ion-beam target. Neutral and ion fragments are then separated in flight time using a static electric field from the spectrometer. They are subsequently measured in coincidence and their momentum imaged using a position- and time-sensitive detector.

quadrupole lenses) were used to collimate the beam. To switch ion beams from H_2^+ to D_2^+ or HD^+, the gas in the source was exchanged.

To separate the H_2^+ from other ion constituents in the beam, the beam was passed through consecutive 25° and 60° mass-selection magnets. These, in addition to electrostatic horizontal and vertical deflectors, were used to steer the beam. A pair of four-jaw slits defined the final path and size of the beam. We estimate the cross-section of the ion beam at the laser interaction point to be about $0.6 \times 0.6\ \text{mm}^2$.

The laser and ion beams were crossed at 90° to one another, as depicted in Fig. 2. The crossing occurred in the presence of a static electric field applied in the direction of ion beam propagation using an axial electrostatic spectrometer. The focus of the laser could be scanned in the direction of the laser propagation to provide intensity control through an intensity-selective scan (ISS) technique [57]. That is, if the ion beam crossed the central portion of the laser focus, the highest intensity obtainable was sampled. If the ion beam crossed an off-center portion where the laser was more de-focused, it sampled a lower intensity but larger interaction volume. This technique has the benefit that, at low intensity where dissociation and ionization rates typically fall off quite rapidly, the signal was enhanced by the larger interaction volume. A detailed comparison between the ISS technique and the more traditional power attenuation method [32] used to control intensity has been reported by Sayler *et al.* [58]. The results show that the two methods are consistent with one another.

Molecules that interact with the laser typically dissociate ($H_2^+ + n\hbar\omega \rightarrow H^+ + H$), or are ionized, resulting in Coulomb explosion ($H_2^+ + n\hbar\omega \rightarrow H^+ + H^+ + e^-$). These mechanisms impart kinetic energy, known as KER, to the fragments. If a molecule is aligned along the ion-beam propagation direction, the KER will result in a time spread between the first and second fragments to reach the detector shown in Fig. 2. In other words, in the center-of-mass frame of the molecule, one fragment gets a "kick" toward the detector from the breakup, while the other gets a kick away from it (due to momentum conservation). If instead the molecule is aligned perpendicular to the ion-beam direction, the KER results in a spatial spread of the fragments in the plane orthogonal to the ion beam. By measuring the time and position of the fragments using a microchannel plate and delay-line anode detector, the angle between the molecular breakup axis and the laser polarization, θ, and the KER can be retrieved (i.e., the three-dimensional momenta of the fragments is calculated). In addition to detecting each hit we require a coincidence between a pair of fragments for a true event to be recorded. Furthermore, momentum conservation is imposed to reduce random coincidences.

The electric field in the interaction region is important because it accelerates the charged fragments (i.e., H^+) toward the detector while not affecting the neutral fragments. In this way, the H^+ ions are separated clearly from the H atoms in flight time to the detector. Thus, a coincidence between H^+ and H denotes a dissociation event, while H^+ and H^+ denotes an ionization event. Similarly, for HD^+, the dissociation channel $H^+ + D$ is distinguished from $H + D^+$ and from ionization, $H^+ + D^+$.

III. RESULTS AND DISCUSSION

A. Dissociation

The strong-field dissociation dynamics of H_2^+ have been studied extensively in the past (see, e.g., Ref. [1] and references therein), particularly for pulses that are longer than a few cycles. Often the best representation to describe the dynamics has been the dressed-states Floquet picture (e.g., Ref. [59]). While strictly speaking this is a continuous-wave model, it nevertheless provides useful insight for ultrashort pulses. The

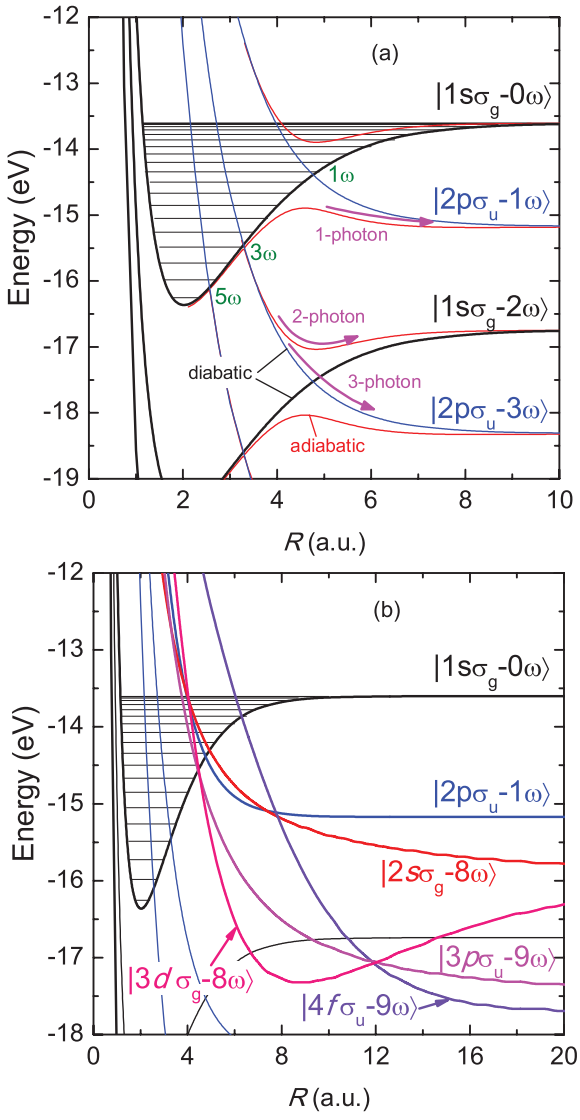

FIG. 3. (Color online) (a) Dressed-states potential energy curves of H_2^+, showing the diabatic and adiabatic curves at $1 \times 10^{13}\ \text{W/cm}^2$. The notation $|2p\sigma_g - 1\omega\rangle$ indicates the $2p\sigma_u$ state dressed by one photon, for example. The labels 1ω, 3ω, and 5ω denote the curve crossings of $2p\sigma_u$ with the $1s\sigma_g$ ground state. Calculated unperturbed vibrational levels are shown by the horizontal lines. (b) Same as (a) but for diabatic curves only and including the dressed H($2l$) states.

dressed-states representation is completely equivalent to that shown in Fig. 1 but, instead of illustrating excitation steps using photons, the Born-Oppenheimer potential energy curves are dressed with the net number of photons absorbed.

Figure 3(a) shows the diabatic and adiabatic dressed-states of H_2^+ at 1×10^{13} W/cm^2—we refer the reader to Refs. [60,61] for more information on the dressed-states Floquet approach. The advantage of the dressed-states representation is that it allows us to track the dissociation pathway of a molecule more easily. For example, the net two-photon pathway shown in Fig. 1, involving three-photon absorption at resonance R_3 followed by one-photon emission at resonance R_1, is easily traceable in Fig. 3(a). First the population emerges through the $|1s\sigma_g - 0\omega\rangle \rightarrow |2p\sigma_g - 3\omega\rangle$ crossing [labeled 3ω in Fig. 3(a)] and then follows the adiabatic route to the asymptotic two-photon limit, $|1s\sigma_g - 2\omega\rangle$. We will use this representation exclusively throughout the rest of our discussion.

In Fig. 4 we present measured KER and angular ($\cos\theta$) distributions for the dissociation of H_2^+ (left column), HD^+ (middle column), and D_2^+ (right column) beams using 7 fs pulses as a function of intensity, as indicated on the figure. Recall that θ is the angle between the laser polarization and the measured fragmentation axis of the molecule. The counts are binned as a function of $\cos\theta$ since an isotropic spherical distribution is uniform in that representation [33]. The composite figure maps out two trends: the KER-$\cos\theta$ distributions as a function of intensity and as a function of nuclear mass. In essence we find an enhancement in high-order ATD with an increase in both parameters that is described in the discussion that follows.

1. Low intensity

We begin with H_2^+ dissociation at 2×10^{13} W/cm^2 [Fig. 4(d)]. Note that this experimental intensity refers to the peak intensity of the focal volume. There are unavoidable contributions to the spectra from lower intensities due to focal-volume averaging (see, e.g., Refs. [1,32]), although the narrow width of our ion beam helps to limit this.

For low intensity, the dominant dissociation mechanism is a one-photon transition from the $1s\sigma_g$ state to the $2p\sigma_u$ state. This can be viewed as a transfer of population from $|1s\sigma_g - 0\omega\rangle \rightarrow |2p\sigma_u - 1\omega\rangle$ through the 1ω crossing in Fig. 3(a). Vibrational states ($v \sim 9$ for H_2^+) with energy near the 1ω crossing (at $R = 4.8$ a.u.) dissociate early in the laser pulse. These states result in an expected KER centered about 0.8 eV in accordance with the peak of the distribution in Fig. 4(d). This KER value is obtained by simply taking the energy difference between the 1ω crossing energy and the asymptotic limit of the $|2p\sigma_u - 1\omega\rangle$ state. Moreover, because it is a simple one-photon transition, one expects the angular distribution for $v = 9$ dissociation to closely follow a $\cos^2\theta$ distribution [28,29,33], in good agreement with that measured [see, for example, Fig. 10(d)].

As the intensity of the laser pulse increases on its leading edge, the gap at the 1ω crossing widens, leading to bond softening [24,62,63]. This process allows states with energy below the 1ω crossing to dissociate. This gap is responsible for the diamond-like shape in the KER-$\cos\theta$ plot centered at KER = 0.8 eV; that is, states below the resonance ($v = 5$–8) result in lower KER while those above it ($v = 10$–13) result in higher KER. The narrowing of the angular distribution on

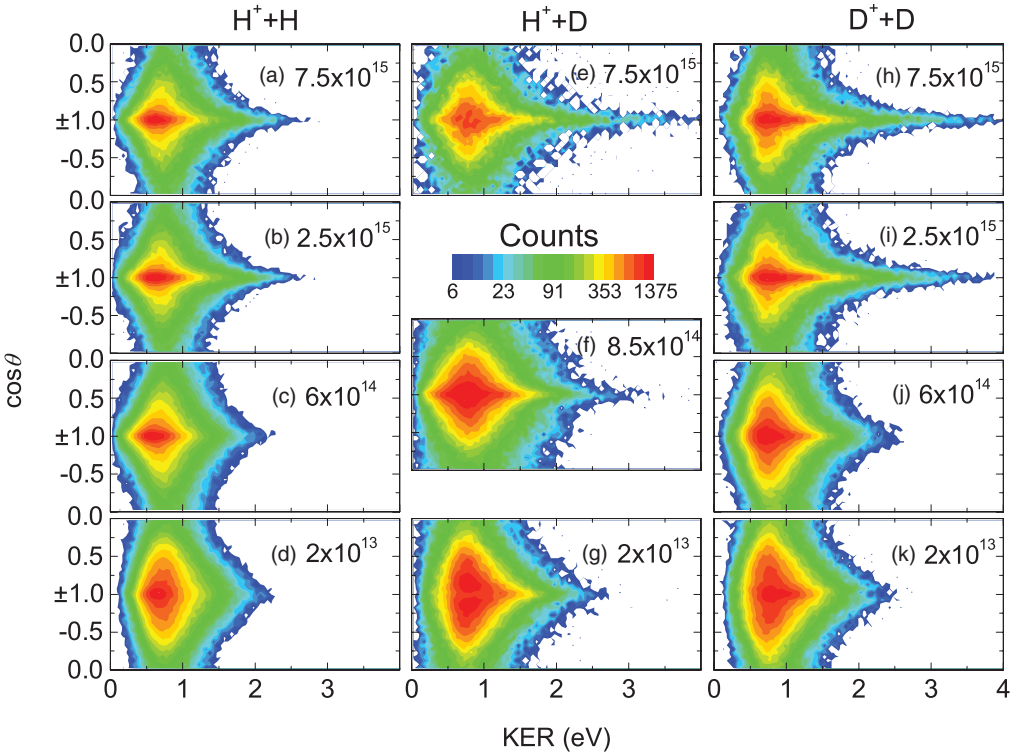

FIG. 4. (Color online) Experimental KER-$\cos\theta$ density plots of dissociation of H_2^+ [(a)–(d)], HD^+ [(e)–(g)], and D_2^+ [(h)–(k)] at intensities indicated (in W/cm^2) for 7 fs, 800 nm laser pulses.

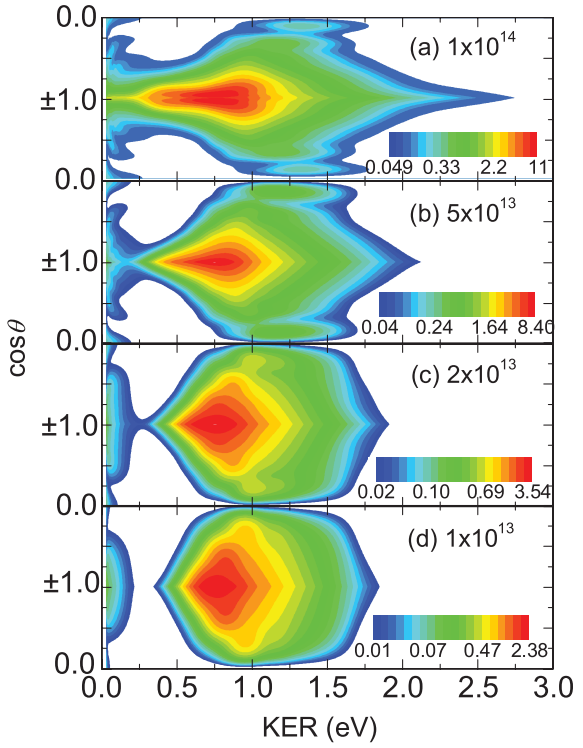

FIG. 5. (Color online) Theoretical KER-cosθ density plots of dissociation of H_2^+ using 7 fs pulses at intensities indicated (in W/cm^2). The false-color scale denotes the dissociation probability density. The data are plotted over the same dynamic range as the experiment in Fig. 4.

either side of the $v = 9$ energy due to bond softening can be explained by the need for higher intensity for those states to dissociate. In these cases, molecules more aligned to the laser polarization will preferentially dissociate, where the intensity component along the internuclear axis is largest, commonly referred to as geometric alignment [64] (the effective intensity along the molecular axis is given by $I_{\text{eff}} = I\cos^2\theta$, where I is the peak intensity).

The behavior observed in the experiment is confirmed by our theoretical calculations shown in Fig. 5. While experiment and theory should not be directly compared, because these theoretical plots neglect the effects of volume averaging, the gross features are similar; for example, both display the aforementioned diamond-like structure at low intensity. It is indeed shown by the theory at 1×10^{13} W/cm^2 in Fig. 6, which shows the individual contributions from different channels, that the main diamond shape arises from a one-photon process since the final population in the relevant KER range ends up on the $2p\sigma_u$ state (following a one-photon transition from $1s\sigma_g$). The separate peak near 0 eV in the calculations is due to a process referred to as zero-photon dissociation [65,66]. However, in the present experiment, this peak could not be measured due to the influence of the Faraday cup (which blocked the low-momentum fragments). Further studies of this feature will be presented elsewhere [67].

Above-threshold dissociation is already evident in the theory for 1×10^{13} W/cm^2 in the narrow pointed tail visible in Fig. 5(d) near KER = 1.75 eV. While it may belong to a one-photon dissociation, this tail can also be the sign of

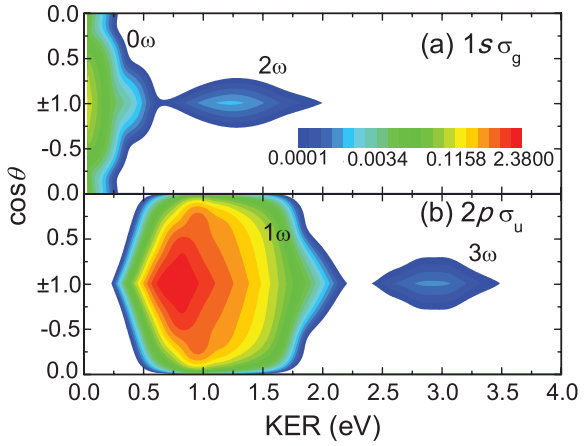

FIG. 6. (Color online) Theoretical KER-cosθ density plots of dissociation of H_2^+ using 7 fs pulses at 1×10^{13} W/cm^2. The false-color scale denotes the dissociation probability density. (a) The $1s\sigma_g$ dissociation probability which includes zero-photon (0ω) and two-photon (2ω) dissociation. (b) The $2p\sigma_u$ dissociation probability, including one-photon (1ω) and three-photon (3ω) dissociation. Note that the dissociation probability density in this plot spans a range two orders of magnitude greater than that in Fig. 5(d).

net two-photon or direct three-photon ATD, explained as follows: In the net two-photon process, population transfers from $|1s\sigma_g - 0\omega\rangle$ to $|2p\sigma_u - 3\omega\rangle$ by three-photon absorption, with the subsequent emission of a photon to $|1s\sigma_g - 2\omega\rangle$—see the adiabatic pathway illustrated in Fig. 3(a). In the direct three-photon process, rather than emitting a photon, the population follows the diabatic path and stays on the $|2p\sigma_u - 3\omega\rangle$ state.

Inspection of the KER-cosθ plots for the individual states, shown in Fig. 6, indicates that the portion responsible for the pointed tail in Fig. 5(d) is predominantly one-photon dissociation along $2p\sigma_u$ but with some contribution from two-photon ATD along $1s\sigma_g$. There is additionally a contribution at higher KER from three-photon ATD along $2p\sigma_u$ that is not visible in Fig. 5(d) due to the chosen lower limit of the color scale. The three-photon contribution is clearly visible in the KER distributions in Fig. 7(d) and has an amplitude similar to that of the two-photon process.

In the theory for 2×10^{13} W/cm^2, the pointed KER tail in Fig. 5 begins to grow. The tail at this intensity is a combination of two-photon and three-photon ATD, as both processes increase in amplitude and start to merge in KER as seen in Fig. 7. This would suggest that the similar feature seen in the experiment at this same intensity [Fig. 4(d)] is likewise a mixture of two-photon and three-photon ATD. Since it requires more photons than one-photon dissociation, ATD requires higher intensity and, therefore, preferentially dissociates the molecules that are aligned along the laser polarization, accounting for the angular narrowness of the feature. This high-energy part of the spectra will remain the main focus of our discussion on ATD.

2. *High intensity*

As the experimental intensity increases in Fig. 4 for H_2^+ from 2×10^{13} to 7.5×10^{15} W/cm^2 in Figs. 4(d) through 4(a),

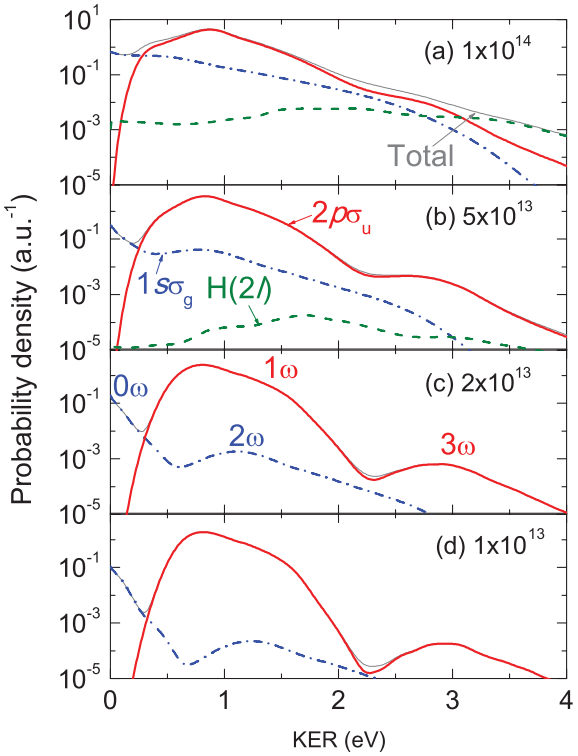

FIG. 7. (Color online) Theoretical KER distributions for dissociation of H_2^+ using 7 fs pulses at intensities indicated (in W/cm^2). The labels in panel (b) denote the final electronic states and are the same for all panels. The labels in panel (c) indicate to which photon process the peaks correspond.

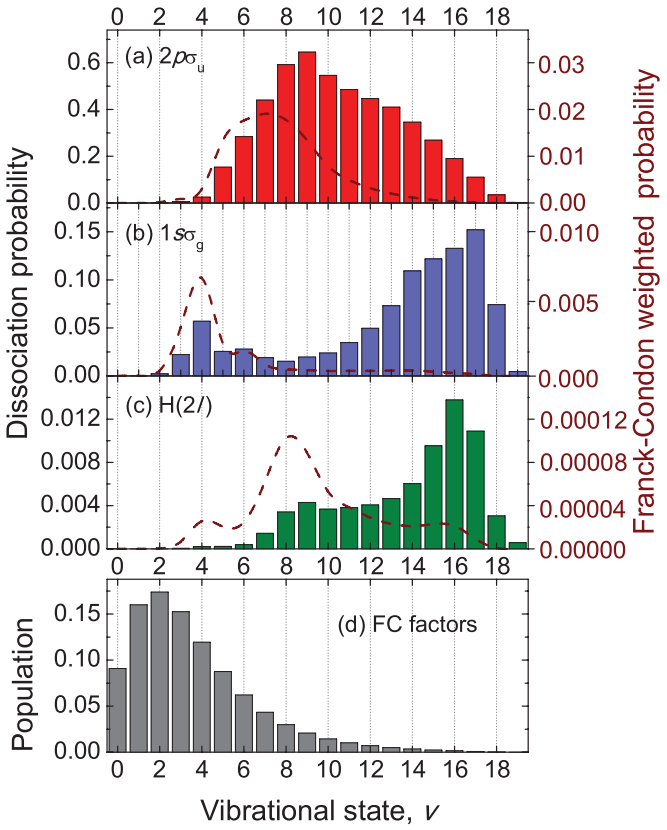

FIG. 8. (Color online) (a)–(c) The solid bars show the calculated dissociation probabilities (left axis) of H_2^+ vibrational states using 7 fs, 1×10^{14} W/cm^2 pulses leading to dissociation on the (a) $2p\sigma_u$, (b) $1s\sigma_g$, and (c) H($2l$) electronic states. The dashed lines show the Franck-Condon weighted probabilities (right axis); that is, the product of the dissociation probability times the Franck-Condon population [see panel (d)]. (d) Franck-Condon population distribution of H_2^+ vibrational states.

two distinct trends are observed. The maximum KER progressively gets larger while the distributions, as a whole, become more aligned. Indeed, at 2.5×10^{15} W/cm^2 it appears that this trend has saturated because there are no further apparent changes in the spectra following the intensity increase to 7.5×10^{15} W/cm^2.

Again using theory to guide us (Figs. 5 and 7), the increase in the high KER cutoff is the signature of further ATD occurring. Surprisingly, the ATD can come from two possible sources, as first discussed in [22]: coupling between the $1s\sigma_g$ and $2p\sigma_u$ states of the H($1l$) manifold (as just discussed), or coupling with the much more highly excited H($2l$) manifold of states (see the upper-lying states in Fig. 1).

Referring to Fig. 7, for 1×10^{13} to 5×10^{13} W/cm^2, the main ATD source is two-photon and three-photon dissociation. At 1×10^{14} W/cm^2 there is an additional non-negligible source of dissociation from the H($2l$) states. This might be considered unexpected because the H($2l$) states lie much higher in energy than the H($1l$) states ($\sim$10 eV) and, therefore, are much harder to reach. However, as Fig. 7(a) shows, for KER > 3.2 eV, the H($2l$) states are the dominant source of dissociation, although after focal-volume averaging of intensities to better represent the experiment, their relative contribution will be smaller.

To examine closely the source of dissociation for different electronic states, Figs. 8(a)–8(c) show the dissociation probability (solid bars) of three H_2^+ vibrational states at 1×10^{14} W/cm^2, leading to the different final electronic states. Note that, for an ion-beam experiment, the individual vibrational state contributions sum incoherently to produce the final spectra.

In Fig. 8(a) dissociation along $2p\sigma_u$ is peaked at $v = 9$ corresponding to one-photon dissociation with only a small dissociation probability for $v = 3$ and $v = 4$ coming from three-photon dissociation.

The $1s\sigma_g$ state, on the other hand [Fig. 8(b)], displays a peak at $v = 4$ from net two-photon dissociation (through the 3ω crossing) and a second larger peak at $v = 17$ coming from below-threshold dissociation; specifically, zero-photon dissociation [65,66]. We note that, although the dissociation probability of the high-v states is larger in this case, their population is much smaller than for the low-v states, as shown by the Franck-Condon population distribution in Fig. 8(d). Thus, the Franck-Condon weighted contribution (probability times Franck-Condon population) from the high-v states will not be as large in the final spectra as shown by the dashed curves in Figs. 8(a)–8(c).

For the H($2l$) states [Fig. 8(c)], two peaks are observed in the dissociation probability distribution. The first is at $v = 9$ and the second is at $v = 16$. The peak at $v = 16$ is likely due to a direct transition from the $1s\sigma_g$ state to a H($2l$) state, such as

$4f\sigma_u$ following the absorption of nine photons, as illustrated on the Floquet diagram incorporating the H($2l$) states shown in Fig. 3(b). For high v, the energy gap to the H($2l$) states is smaller, making direct transitions more likely. The peak at $v = 9$ may similarly involve a direct transition, or alternatively involve a two-step dissociation process. The two-step process is initiated by bond softening through the 1ω crossing with $2p\sigma_u$. Then, at larger R where the energy gap to the H($2l$) states is smaller, the population is further excited to a H($2l$) state, such as $2s\sigma_g$ following the additional absorption of seven photons. This is the same mechanism that Gibson *et al*. report to have observed [68].

Looking more specifically at the $v = 1$, 3, and 9 states of H_2^+ that are nearest in energy to the 5ω, 3ω, and 1ω crossings in Fig. 3(a), respectively, their final KER distributions at 1×10^{14} W/cm^2 are shown in Fig. 9. We note that, in general, the peaks for all of the spectra are quite broad in KER due to the large bandwidth (~0.5 eV) of the short laser pulses.

For $v = 1$ [Fig. 9(a)], the $2p\sigma_u$ state displays a broad peak centered at KER ~ 2 eV. This peak can be ascribed to net three-photon dissociation through either the 3ω or 5ω crossings, identified based on KER. The $1s\sigma_g$ state displays one peak below 1 eV for net two-photon dissociation via the 3ω crossing and a second peak at ~3.5 eV from net four-photon dissociation via the 5ω crossing. The H($2l$) contribution is negligible for $v = 1$.

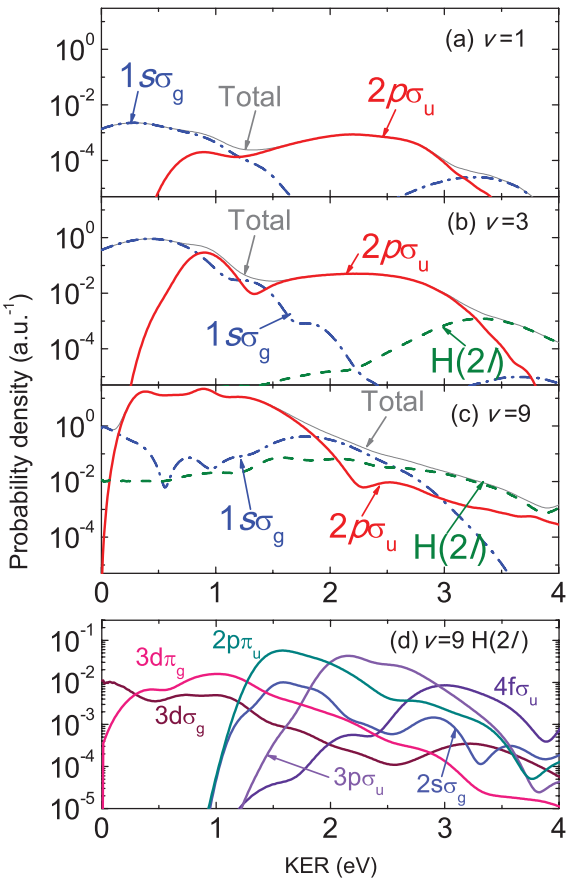

FIG. 9. (Color online) Theoretical KER distributions for select vibrational states of H_2^+ using 7 fs, 1×10^{14} W/cm^2 pulses: (a) $v = 1$, (b) $v = 3$, and (c) $v = 9$. (d) The individual contributions from the H($2l$) states are shown for $v = 9$. The labels denote the final electronic states.

For $v = 3$ [Fig. 9(b)], the $2p\sigma_u$ state shows a peak similar to $v = 1$ and is again from three-photon dissociation through the 3ω crossing. For $1s\sigma_g$, the peak observed at 3.5 eV for $v = 1$ is suppressed for $v = 3$ since four-photon dissociation is much less likely for $v = 3$ because this state is farther from the 5ω crossing than $v = 1$. Dissociation on the H($2l$) states is now visible at high KER and is indeed dominant at the highest KER.

In contrast to the lower-v states, the spectra for $v = 9$ [Fig. 9(c)] are dramatically different. The $2p\sigma_u$ state shows a dominant peak centered just below 1 eV from one-photon dissociation. The $1s\sigma_g$ state shows a peak at zero energy from below-threshold dissociation and a peak at 2 eV from two-photon dissociation. The H($2l$) excited states now display multiple peaks over a broad range of KER, clearly identifiable in the individual H($2l$) state contributions shown in Fig. 9(d). These peaks can be assigned to ATD from the H($2l$) states where a net sum of 8 or more photons are absorbed.

As an example, for $v = 9$, we attempt to relate some of the observed peaks in the H($2l$) spectra to specific dissociation pathways in the Floquet diagram in Fig. 3(b). The energy difference between $v = 9$ and the $|3d\sigma_g - 8\omega\rangle$ and $|2s\sigma_g - 8\omega\rangle$ dissociation limits is 1.6 eV. The $2s\sigma_g$ state in Fig. 9(d) has a large dissociation peak at ~1.6 eV consistent with the Floquet pathway, while the $3d\sigma_g$ state is inconsistent, peaking rather at 0 eV and again at 3.2 eV. Indeed, this spacing is the energy of two photons, suggesting ATD transitions to this state.

From Floquet, the pathways involving $|4f\sigma_u - 9\omega\rangle$ and $|3p\sigma_u - 9\omega\rangle$ should both give a KER of 3.2 eV. This value seems to agree with the main peak for $4f\sigma_u$ but is somewhat higher than the broad peak centered at ~2.5 eV for $3p\sigma_u$. So, in general, some of the assignments from the Floquet pathways work well but others are less agreeable—possibly because they involve more complicated mixing of pathways.

Overall, we can draw two conclusions from the theoretical spectra (see also Ref. [22]). First, despite the H($2l$) states often being omitted from calculations, our calculations show that, at high intensity, not only may dissociation occur along the H($2l$) states, but there are also ATD peaks associated with these peaks. In particular, for high KER, the H($2l$) states are the dominant dissociation channel. Second, the tail observed in the experimental H_2^+ KER-cosθ plot in Fig. 4(a) extending to above 2.5 eV is likely to be from a mixture of two-photon, three-photon, and H($2l$) ATD, although the relative contribution of the latter channel is reduced due to focal-volume averaging.

3. *Angular dependence*

The narrowing of the H_2^+ dissociation angular distributions for increasing intensity seen in the experimental KER-cosθ plots is demonstrated in the one-dimensional (1D) angular plots in Fig. 10. In these plots, the dissociation yield has been integrated across all KER. At 2×10^{13} W/cm^2 the distribution follows cos$^2\theta$ consistent with the fact that the dominant contribution is from one-photon dissociation. For higher intensity, this broad underlying cos$^2\theta$ distribution

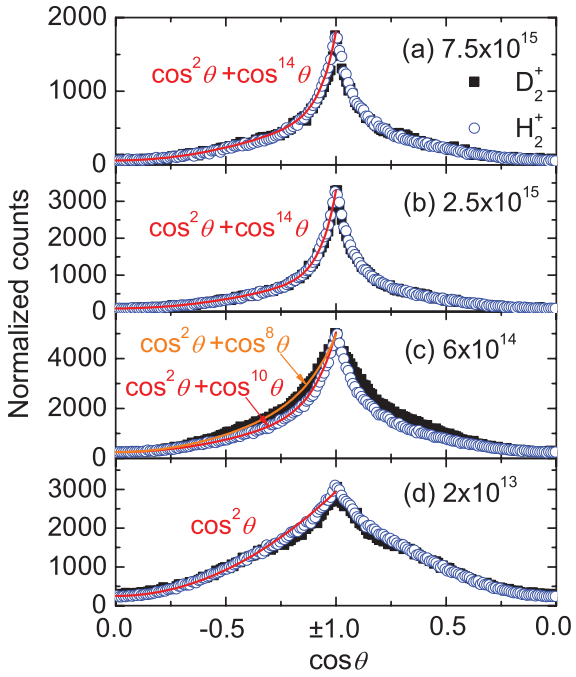

FIG. 10. (Color online) Experimental angular distributions for H_2^+ and D_2^+ dissociation, integrated over all KER, using 7 fs pulses at the intensities indicated. The data (symbols) are fit with $\cos^n\theta$ distributions (solid lines) as marked. The H_2^+ and D_2^+ distributions are normalized to each other's peak.

persists as vibrational states near the 1ω crossing continue to dissociate on the leading edge of the laser pulse, and also from low-intensity, high-volume contributions due to focal-volume averaging. However, on top of this $\cos^2\theta$ distribution there appears a narrower ridge. At 6×10^{14} W/cm^2, it is fit with $\cos^{10}\theta$ for H_2^+ (open circles) while at 2.5×10^{15} W/cm^2 it is fit with $\cos^{14}\theta$, with the order of fit chosen empirically to give the best agreement with the data. It does not appear to become any narrower above 2.5×10^{15} W/cm^2.

This angular trend with intensity is also reproduced qualitatively by the calculations (see Fig. 5)—although the narrowing is more pronounced in the theory, likely because the intensity averaging was not performed. The calculations reveal that there are two reasons for the narrowing:

First, the onset of higher-order ATD processes at higher intensity naturally leads to a more aligned angular distribution since only the most aligned molecules effectively experience the highest intensity along the molecular bond, often referred to as geometric alignment. The second explanation involves molecular rotation. At high intensity, more and more photons are continuously absorbed and emitted. Each absorption and emission step adds (or subtracts) angular momentum to (from) the molecules, exciting a broader range of rotational J states of the system. For the calculations at 1×10^{14} W/cm^2 we find rotational excitation up to about $J = 40$. Physically, the laser torques the molecules and induces rotational motion. This tends to align the molecules along the laser polarization, a process often referred to as dynamic alignment [64]. Our calculations show that alignment may indeed occur after the pulse [69].

Additionally, there is experimental and theoretical evidence that the alignment depends on the nuclear mass. For example, at 6×10^{14} W/cm^2, experimental data in Fig. 10(c) shows that the narrow ridge of D_2^+ ($\cos^8\theta$) is slightly broader than that of H_2^+ ($\cos^{10}\theta$), although there does not appear to be any significant differences at the other intensities we have explored. Our calculations also show substantial differences between H_2^+ and D_2^+ where, in the comparison with Figs. 12(a)–12(c) and 12(d)–12(f), D_2^+ is clearly much broader in angle than H_2^+ for all pulse durations.

4. *Nuclear mass*

Returning our attention to Fig. 4, we now compare the experimental differences in dissociation for H_2^+, HD^+, and D_2^+. Aside from the small differences in angular distribution already described, at high intensity the more massive isotopologues display a much larger high-KER tail. This is emphasized in the 1D KER plots in Fig. 11 where D_2^+ at 7.5×10^{15} W/cm^2 shows a tail extending to 4 eV compared to H_2^+ whose tail falls off to a similar amplitude below 3 eV.

As identified from our theory, the high KER is predominantly evidence for high-order ATD through the H($1l$) states with some contribution from the H($2l$) states. The mechanism for the additional high-order ATD in D_2^+ was discussed briefly in the introduction. Since D_2^+ is the most massive isotopologue, its nuclear wave packet requires longer to travel a given distance. For example, for D_2^+ dissociating on $|2p\sigma_u - 3\omega\rangle$, if the laser pulses are sufficiently short, the $|2p\sigma_u - 3\omega\rangle \rightarrow |1s\sigma_g - 2\omega\rangle$ crossing will be closed before the D_2^+ wave packet can reach it. This leaves the D_2^+ wave packet on the $|2p\sigma_u - 3\omega\rangle$ state to follow the diabatic path to direct three-photon ATD yielding a higher KER. The H_2^+

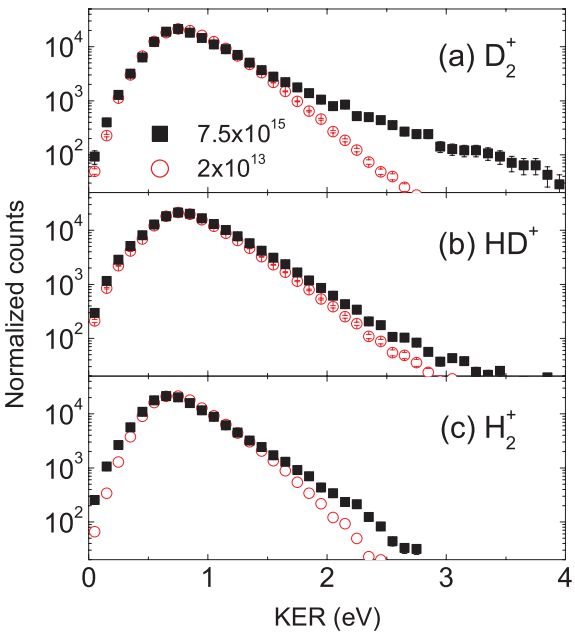

FIG. 11. (Color online) Experimental KER distributions for (a) D_2^+, (b) HD^+, and (c) H_2^+ using 7 fs pulses at $2 \times 10^{13}$and 7.5×10^{15} W/cm^2 corresponding to the plots in Fig. 4. The distributions are all normalized to their peak values. Error bars denote the statistical error in the data.

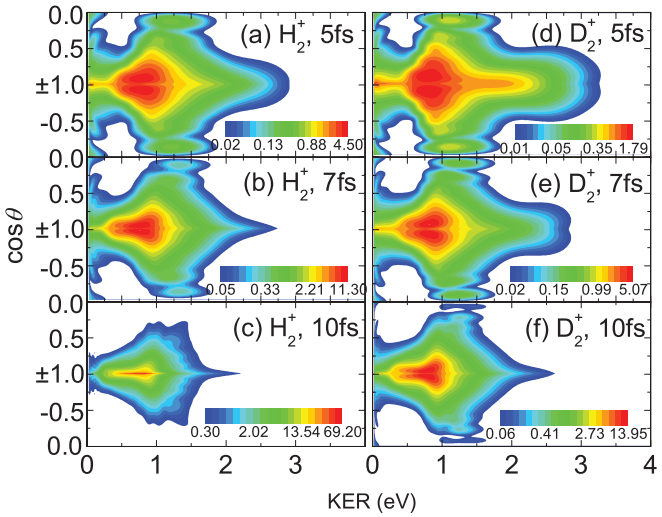

FIG. 12. (Color online) Theoretical KER-cosθ distributions for [(a)–(c)] H_2^+ and [(d)–(f)] D_2^+ at 1×10^{14} W/cm^2 and pulse durations of 5, 7, and 10 fs as indicated. The color bar denotes the probability density. Plots for H_2^+ and D_2^+ are over the same dynamic range.

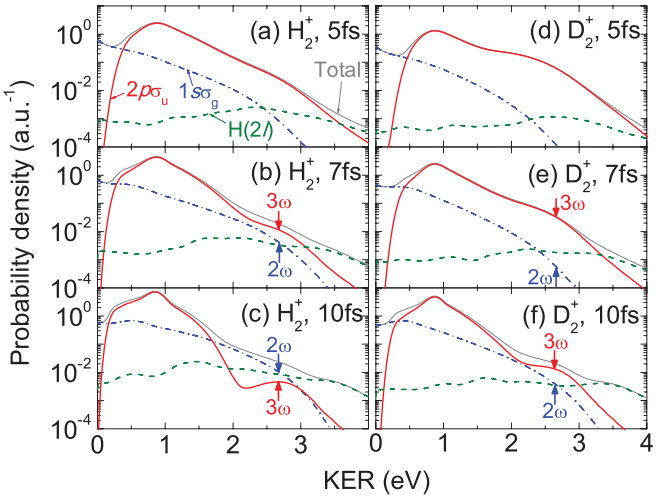

FIG. 13. (Color online) Calculated KER distributions for [(a)–(c)] H_2^+ and [(d)–(f)] D_2^+ at 1×10^{14} W/cm^2 and pulse durations of 5, 7, and 10 fs as indicated. The labels in panel (a) denote the final electronic state and are the same used for all panels.

ion, on the other hand, is less massive and stretches faster than D_2^+. It requires less time to reach the $|2p\sigma_u - 3\omega\rangle \rightarrow |1s\sigma_g - 2\omega\rangle$ crossing and is therefore more likely to follow the adiabatic path and end up with net two-photon ATD. As a result, D_2^+ can be expected to display more high-order ATD than H_2^+, consistent with the findings in Figs. 4 and 11 (see also theory in Ref. [70]). In HD^+, the effect is in between that of H_2^+ and D_2^+. This is further affirmed by the observation that, at low intensity (2×10^{13} W/cm^2), the distributions of all three isotopologues look more similar (Fig. 11) because very little ATD occurs and the distributions are dominated by one-photon dissociation which is relatively independent of the nuclear mass.

The qualitative differences between H_2^+ and D_2^+ are reproduced fairly well by theory. Figures 12(b) and 12(e), and 13(b) and 13(e), compare H_2^+ and D_2^+ dissociation at 7 fs, 1×10^{14} W/cm^2. Concentrating on the KER range between 2.0 and 3.5 eV, Fig. 13 shows that, for D_2^+, in comparison to H_2^+, the $1s\sigma_g$ two-photon contribution diminishes while the $2p\sigma_u$ three-photon contribution increases [see regions marked by arrows in Figs. 13(b), 13(c), 13(e), and 13(f) as an example]. This indicates that the diabatic three-photon pathway for D_2^+ is enhanced at the expense of the adiabatic two-photon pathway. In fact, Fig. 14, which directly compares dissociation along $2p\sigma_u$, shows that, for the same pulse duration, the relative amount of three-photon ATD (~2–3.5 eV) is approximately an order of magnitude higher for D_2^+ than for H_2^+.

5. *Pulse duration*

It is also interesting to compare the dependence of high-order ATD on pulse duration. Since the enhancement of the high-order ATD is purely a temporal effect—D_2^+ having less time than H_2^+ to follow the lower-order adiabatic pathways—for shorter pulses we also expect more high-order ATD [22]. This is precisely what the theory shows. With decreasing pulse duration three-photon ATD is enhanced (see, e.g., Fig. 14). Moreover, as shown by Hua and Esry [71], and by Madsen [72], the "effective" pulse duration scales with the square root of the nuclear mass ratio. For example, since D_2^+ is twice as massive as H_2^+, it dissociates $\sqrt{2}$ slower. Thus, D_2^+ in a 10 fs pulse behaves similarly to H_2^+ in a 7 fs pulse, as seen in Figs. 12 and 14. Likewise, D_2^+ in a 7 fs pulse is equivalent to H_2^+ in a 5 fs pulse. This provides an attractive, although somewhat limited, way to access the physics of extremely short pulses without needing to produce them, which is still technically rather challenging.

To test the pulse duration dependence we repeated the experiments on D_2^+ but at 10 fs and compared them with those at 7 fs in Fig. 15. At both 6×10^{14} and 7.5×10^{15} W/cm^2, the 7 fs results show a larger contribution at higher KER consistent with the theoretical predictions. This seems to confirm the link between the high KER that comes from high-order ATD and

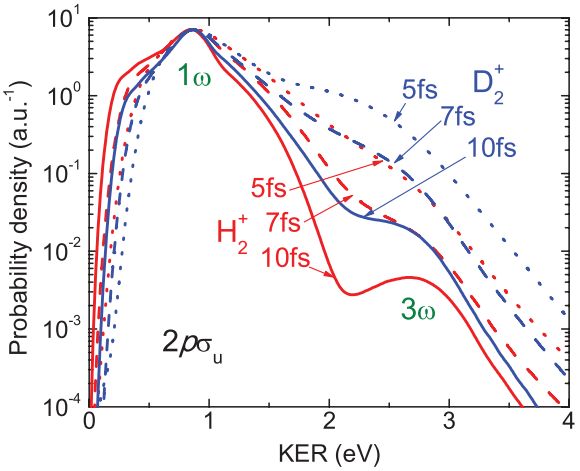

FIG. 14. (Color online) Comparison of the calculated KER distributions for dissociation on the $2p\sigma_u$ state of H_2^+ and D_2^+ at 1×10^{14} W/cm^2 and pulse durations of 5, 7, and 10 fs as indicated. The distributions are all normalized to the peak of the H_2^+, 10 fs total probability density.

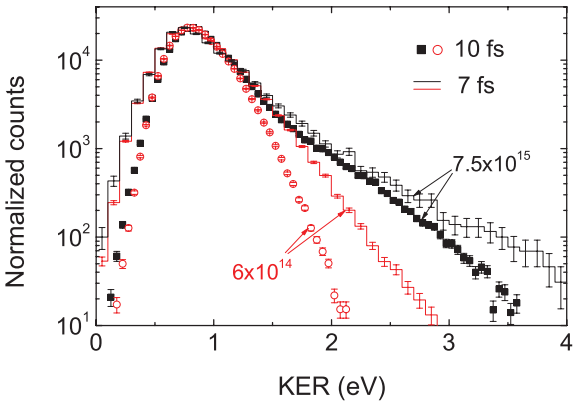

FIG. 15. (Color online) Experimental KER distributions for dissociation of D_2^+ using 7 and 10 fs pulses at 6×10^{14} and 7.5×10^{15} W/cm^2 as indicated. The distributions are all normalized to their peak values. Error bars denote the statistical error in the data.

the effective time for dissociation. For either shorter pulses or more massive systems the nuclear wave packet has less time to follow the adiabatic dissociation route and is forced into the higher-order ATD channels. It is important to bear in mind that the larger bandwidth of the shorter laser pulses can have an effect too. Larger pulse bandwidth can lead to dissociation at smaller internuclear distance and thereby contribute to higher KER, following the trend observed in the experiment. Careful consideration of our theory suggests that this bandwidth effect is likely to be smaller than the effect of the enhanced high-order ATD but cannot be completely discarded.

The mass scaling predicted by theory, however, was not so well reproduced by experiment. When we directly compared the 7 fs H_2^+ data with the 10 fs D_2^+ data (comparison not shown), the dissociation yield at large KER (~3.0 eV) of H_2^+ was below that of D_2^+. It is unclear why, but we note there are many parameters that can influence an accurate direct comparison of the experimental spectra.

B. Ionization

In addition to dissociation, we have also measured the intense-field ionization of H_2^+ and D_2^+ using few-cycle pulses. The KER distributions for 7 fs pulses at a selection of intensities are displayed in Fig. 16 along with KER-cosθ distributions at 7.5×10^{15} W/cm^2. We note that the angular distributions in Figs. 16(d) and 16(e) show that the molecules are preferentially ionized along the laser polarization direction, consistent with our measurements reported in Refs. [30,73]. While our coincidence experimental technique allows us to clearly distinguish dissociation events (ion-neutral coincidence) from ionization events (ion-ion coincidence), the ionization channel does suffer from the possibility of false coincidences due to the much larger rate of dissociation events. That is, if two ions coming from two different dissociation events arrive at the same time and happen to satisfy the momentum conservation conditions imposed in our analysis, they may be mistaken for ionization. This can be particularly problematic since the dissociation channel is dominant when starting from an ion-beam target. Fortunately, these random

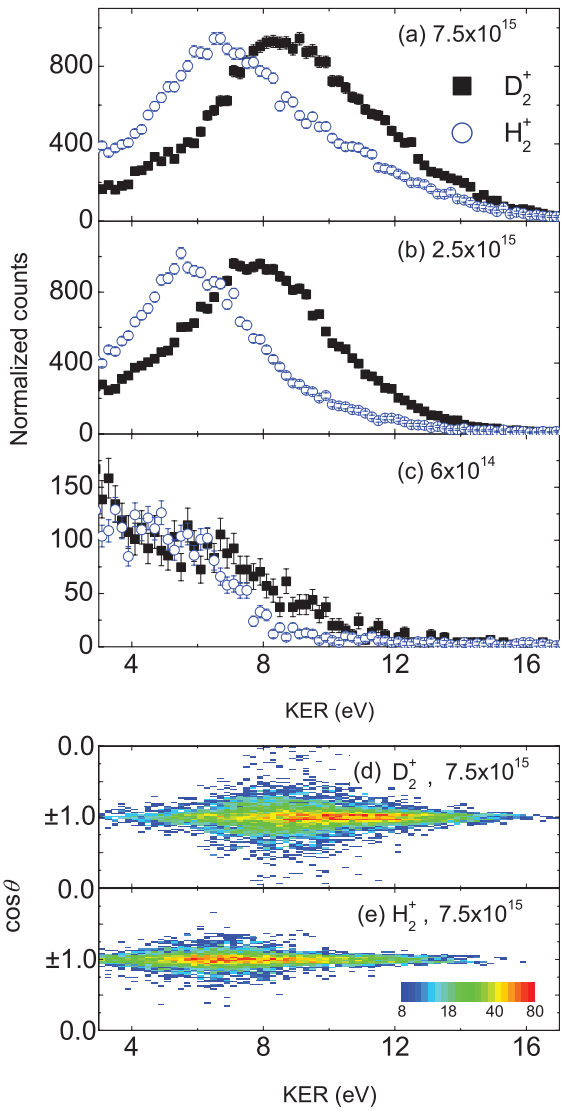

FIG. 16. (Color online) Experimental KER and KER-cosθ distributions for ionization of H_2^+ and D_2^+ (as labeled) using 7 fs pulses at intensities indicated (in W/cm^2). The H_2^+ and D_2^+ distributions are normalized to the peak of each other. Error bars denote the statistical error in the data.

events have "low KER," which is the reason we do not display the spectra below 3 eV in Fig. 16.

In Fig. 16 we observe two trends. The first is that with increasing intensity, the distribution shifts to larger KER (as is also observed in studies of H_2 double ionization [74]). The reason for this shift is easily understood by considering the energy gap between the H($1l$) states of H_2^+ and the $1/R$ ionization threshold as shown in Fig. 1. At low intensity the laser can only excite the molecule to the $1/R$ state at relatively large R where the gap is smaller. Thus, the molecule is likely to start dissociating and stretch before being ionized. Since one-photon dissociation of H_2^+ ion beams can begin early on the leading edge of the laser pulse, the molecules have sufficient time to stretch significantly even with few-cycle pulses. Under the reflection approximation, a KER in the range of 4–7 eV, as observed at 6×10^{14} W/cm^2 [Fig. 16(c)] indicates ionization at $R \sim 4$–8 a.u. [75]. This is in the range

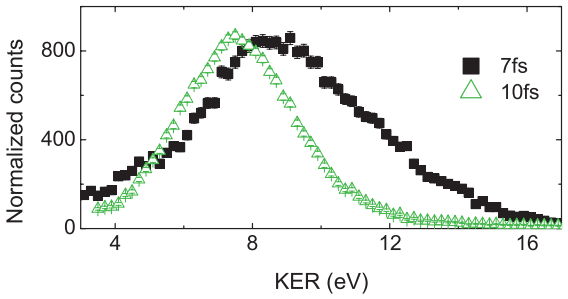

FIG. 17. (Color online) Experimental KER distributions for ionization of D_2^+ using 7 and 10 fs pulses (as labeled) at 7.5×10^{15} W/cm^2. The distributions are normalized to the peak of each other. Error bars denote the statistical error in the data.

of the enhanced ionization predicted for H_2^+ [76–78] and is also consistent with the above-threshold Coulomb explosion peaks observed by Esry *et al.* [73,79]. At higher intensity, ionization to the $1/R$ curve can occur at smaller R where the energy gap is larger. Since the molecules explode from smaller internuclear distance where the nuclear charge repulsion is greater, the KER is larger. Hence, we observe a progressive shift of the distribution to higher KER with increasing intensity.

The second feature we observe is that D_2^+ ionization consistently displays larger KER than H_2^+. This aspect can be assigned to temporal effects. The D_2^+ nuclei are more massive and therefore can stretch less than H_2^+ within the same pulse duration. As a result of stretching less, D_2^+ is ionized at smaller R, giving larger KER. Applying the same reasoning, we predict that shorter pulse durations similarly lead to larger KER (see also H_2 studies [74]). Figure 17 shows the ionization spectra of D_2^+ at 7.5×10^{15} W/cm^2 for 7 and 10 fs pulses. One notices that the spectrum at 10 fs is shifted to lower KER with respect to 7 fs, consistent with the D_2^+ molecules having more time to stretch before the 10 fs pulse peaks.

C. Summary and Outlook

In conclusion, we have presented a study of the dissociation and ionization of hydrogenic molecular-ion beams in few-cycle laser pulses. In particular, the focus has been on the enhancement of high-order (three-photon or more) ATD by using effectively shorter laser pulses [22].

We have shown that, if one can slow down the timescale for dissociation by using a more massive system (i.e., D_2^+), an enhancement of about a factor of ten in three-photon ATD is witnessed at the expense of two-photon ATD. Furthermore, an equivalent enhancement is observed when the pulse length is scaled by the reduced mass. This demonstrates a very simplified form of control whereby one can manipulate the dissociation pathway of a molecule. Additionally, our three-dimensional calculations that describe the experimental results to a high degree indicate a significant fraction of dissociation on the excited H($2l$) states at 1×10^{14} W/cm^2, thus illustrating the importance of including these states in future calculations at high intensity. Moreover, there are a number of other intriguing features in the data—for example, the theory predicts strong dynamic alignment using few-cycle pulses, an effect for which we found tentative evidence in our experiment.

In the measurements of ionization of H_2^+ beams using few-cycle pulses, we observe time-dependent effects similar to dissociation. In particular, we find that D_2^+ ionization displays larger KER than H_2^+, which can be assigned to the slower stretching motion of the D_2^+ molecule compared to H_2^+ before ionization. This too is consistent with our observations that the KER is larger for a given isotopologue for shorter pulses.

Looking to the future, there are a number of approaches that could be used to enhance the effectiveness of the simple dissociation control scheme employed here. One obvious approach would be to use a more massive system. While T_2^+ is not practical, there are many other H_2^+-like systems that would be equally good. For example, Ar_2^+ has potential energy curves that in many respects resemble those of H_2^+ and would similarly produce ATD (see light-induced potentials studies by Wunderlich *et al.* [80,81]). Since the timescale for a dissociating Ar_2^+ wave packet to travel between curve crossings is much longer than in H_2^+ (tens of femtoseconds for Ar_2^+), the effect of using a short pulse to enhance high-order ATD is expected to be more dramatic.

Alternatively, we can envision the use of a pump-pump-probe scheme in the near future. An extremely short infrared pulse (a few femtoseconds duration) or even an attosecond xuv pulse could be used to ionize D_2 and launch a well-localized coherent vibrational wave packet in D_2^+. A second short infrared pulse timed to open the 3ω crossing as the wave packet passes through it would initiate three-photon dissociation. Then, the presence or absence of a carefully timed third short infrared pulse could be used to gate the ATD process by steering the wave packet along the two-photon or three-photon pathway.

ACKNOWLEDGMENTS

The authors wish to thank Professor Z. Chang and his group members, and Dr. C. W. Fehrenbach for assistance with the laser and ion beams, respectively. This work was supported by the Chemical Sciences, Geosciences, and Biosciences Division, Office of Basic Energy Sciences, Office of Science, US Department of Energy.

[1] J. H. Posthumus, Rep. Prog. Phys. **67**, 623 (2004).
[2] H. Niikura, V. R. Bhardwaj, F. Legare, I. Litvinyuk, P. Dooley, D. Rayner, M. Y. Ivanov, P. Corkum, and D. Villeneuve, in *Strong Field Laser Physics*, edited by Thomas Brabec (Springer, New York, 2009), Vol. 134, pp. 185–208.
[3] A. H. Zewail, Science **242**, 1645 (1988).
[4] H. Niikura, D. M. Villeneuve, and P. B. Corkum, Phys. Rev. A **73**, 021402(R) (2006).
[5] D. S. Murphy, J. McKenna, C. R. Calvert, W. A. Bryan, E. M. L. English, J. Wood, I. C. E. Turcu, W. R. Newell, I. D. Williams, and J. F. McCann, J. Phys. B **40**, S359 (2007).

[6] T. Niederhausen and U. Thumm, Phys. Rev. A **77**, 013407 (2008).

[7] E. Charron, A. Giusti-Suzor, and F. H. Mies, Phys. Rev. Lett. **75**, 2815 (1995).

[8] E. Charron, A. Giusti-Suzor, and F. H. Mies, J. Chem. Phys. **103**, 7359 (1995).

[9] B. Sheehy, B. Walker, and L. F. DiMauro, Phys. Rev. Lett. **74**, 4799 (1995).

[10] F. He, C. Ruiz, and A. Becker, Phys. Rev. Lett. **99**, 083002 (2007).

[11] D. Ray, F. He, S. De, W. Cao, H. Mashiko, P. Ranitovic, K. P. Singh, I. Znakovskaya, U. Thumm, G. G. Paulus, M. F. Kling, I. V. Litvinyuk, and C. L. Cocke, Phys. Rev. Lett. **103**, 223201 (2009).

[12] K. P. Singh, F. He, P. Ranitovic, W. Cao, S. De, D. Ray, S. Chen, U. Thumm, A. Becker, M. M. Murnane, H. C. Kapteyn, I. V. Litvinyuk, and C. L. Cocke, Phys. Rev. Lett. **104**, 023001 (2010).

[13] G. Sansone, F. Kelkensberg, J. F. Pérez-Torres, F. Morales, M. F. Kling, W. Siu, O. Ghafur, P. Johnsson, M. Swoboda, E. Benedetti, F. Ferrari, F. Lépine, J. L. Sanz-Vicario, S. Zherebtsov, I. Znakovskaya, A. L' Huillier, M. Yu. Ivanov, M. Nisoli, F. Martín, and M. J. J. Vrakking, Nature (London) **465**, 763 (2010).

[14] V. Roudnev, B. D. Esry, and I. Ben-Itzhak, Phys. Rev. Lett. **93**, 163601 (2004).

[15] V. Roudnev and B. D. Esry, Phys. Rev. A **71**, 013411 (2005).

[16] M. F. Kling, Ch. Siedschlag, A. J. Verhoef, J. I. Khan, M. Schultze, Th. Uphues, Y. Ni, M. Uiberacker, M. Drescher, F. Krausz, and M. J. J. Vrakking, Science **312**, 246 (2006).

[17] V. Roudnev and B. D. Esry, Phys. Rev. A **76**, 023403 (2007).

[18] V. Roudnev and B. D. Esry, Phys. Rev. Lett. **99**, 220406 (2007).

[19] M. F. Kling, C. Siedschlag, I. Znakovskaya, A. J. Verhoef, S. Zherebtsov, F. Krausz, M. Lezius, and M. J. J. Vrakking, Molecular Physics **106**, 455 (2008).

[20] X. M. Tong and C. D. Lin, Phys. Rev. Lett. **98**, 123002 (2007).

[21] M. Kremer, B. Fischer, B. Feuerstein, V. L. B. de Jesus, V. Sharma, C. Hofrichter, A. Rudenko, U. Thumm, C. D. Schröter, R. Moshammer, and J. Ullrich, Phys. Rev. Lett. **103**, 213003 (2009).

[22] J. McKenna, A. M. Sayler, F. Anis, B. Gaire, Nora G. Johnson, E. Parke, J. J. Hua, H. Mashiko, C. M. Nakamura, E. Moon, Z. Chang, K. D. Carnes, B. D. Esry, and I. Ben-Itzhak, Phys. Rev. Lett. **100**, 133001 (2008).

[23] M. Machholm and A. Suzor-Weiner, J. Chem. Phys. **105**, 971 (1996).

[24] P. H. Bucksbaum, A. Zavriyev, H. G. Muller, and D. W. Schumacher, Phys. Rev. Lett. **64**, 1883 (1990).

[25] A. Zavriyev, P. H. Bucksbaum, H. G. Muller, and D. W. Schumacher, Phys. Rev. A **42**, 5500 (1990).

[26] J. McKenna, A. M. Sayler, B. Gaire, N. G. Johnson, M. Zohrabi, K. D. Carnes, B. D. Esry, and I. Ben-Itzhak, J. Phys. B **42**, 121003 (2009).

[27] A. Rudenko, B. Feuerstein, K. Zrost, V. L. B. de Jesus, Th. Ergler, C. Dimopoulou, C. D. Schröter, R. Moshammer, and J. Ullrich, J. Phys. B **38**, 487 (2005).

[28] I. D. Williams, P. McKenna, B. Srigengan, I. M. G. Johnston, W. A. Bryan, J. H. Sanderson, A. El-Zein, T. R. J. Goodworth, W. R. Newell, P. F. Taday and A. J. Langley, J. Phys. B **33**, 2743 (2000).

[29] K. Sändig, H. Figger, and T. W. Hänsch, Phys. Rev. Lett. **85**, 4876 (2000).

[30] I. Ben-Itzhak, P. Q. Wang, J. F. Xia, A. M. Sayler, M. A. Smith, K. D. Carnes, and B. D. Esry, Phys. Rev. Lett. **95**, 073002 (2005).

[31] D. Pavičić, A. Kiess, T. W. Hänsch, and H. Figger, Phys. Rev. Lett. **94**, 163002 (2005).

[32] P. Q. Wang, A. M. Sayler, K. D. Carnes, J. F. Xia, M. A. Smith, B. D. Esry, and I. Ben-Itzhak, Phys. Rev. A **74**, 043411 (2006).

[33] P. Q. Wang, A. M. Sayler, K. D. Carnes, J. F. Xia, M. A. Smith, B. D. Esry, and I. Ben-Itzhak, J. Phys. B **38**, L251 (2005).

[34] P. A. Orr, I. D. Williams, J. B. Greenwood, I. C. E. Turcu, W. A. Bryan, J. Pedregosa-Gutierrez, and C. W. Walter, Phys. Rev. Lett. **98**, 163001 (2007).

[35] J. McKenna, M. Suresh1, D. S. Murphy, W. A. Bryan, L.-Y. Peng, S. L. Stebbings, E. M. L. English, J. Wood, B. Srigengan, I. C. E. Turcu, J. L. Collier, J. F. McCann, W. R. Newell and I. D. Williams, J. Phys. B **40**, 2607 (2007).

[36] J. McKenna, A. M. Sayler, B. Gaire, N. G. Johnson, K. D. Carnes, B. D. Esry, and I. Ben-Itzhak, Phys. Rev. Lett. **103**, 103004 (2009).

[37] J. McKenna, F. Anis, B. Gaire, N. G. Johnson, M. Zohrabi, K. D. Carnes, B. D. Esry, and I. Ben-Itzhak, Phys. Rev. Lett. **103**, 103006 (2009).

[38] Vaibhav S. Prabhudesai, Uri Lev, Adi Natan, Barry D. Bruner, Adi Diner, Oded Heber, Daniel Strasser, D. Schwalm, Itzik Ben-Itzhak, J. J. Hua, B. D. Esry, Yaron Silberberg, and Daniel Zajfman, Phys. Rev. A **81**, 023401 (2010).

[39] M. Odenweller, N. Takemoto, A. Vredenborg, K. Cole, K. Pahl, J. Titze, L. P. H. Schmidt, T. Jahnke, R. Dorner, and A. Becker, Phys. Rev. Lett. **107**, 143004 (2011).

[40] P. B. Corkum, Phys. Rev. Lett. **71**, 1994 (1993).

[41] K. J. Schafer, B. Yang, L. F. DiMauro, and K. C. Kulander, Phys. Rev. Lett. **70**, 1599 (1993).

[42] X. M. Tong, Z. X. Zhao, and C. D. Lin, Phys. Rev. Lett. **91**, 233203 (2003).

[43] Maximum field strength in atomic units is defined as $\mathcal{E}_0 = [I/(3.5 \times 10^{16}\ \mathrm{W/cm^2})]^{1/2}$, with I being the laser peak intensity. The full width at half maximum of intensity (τ_{FWHM}) defines τ as $\tau = \tau_{\mathrm{FWHM}}/\sqrt{2\ln 2}$.

[44] B. D. Esry and H. R. Sadeghpour, Phys. Rev. A **60**, 3604 (1999).

[45] F. Anis and B. D. Esry, Phys. Rev. A **77**, 033416 (2008).

[46] F. Anis, Ph.D. thesis, Kansas State University (2009).

[47] S. J. Singer, K. F. Freed, and Y. B. Band, J. Chem. Phys. **79**, 6060 (1983).

[48] S. J. Singer, K. F. Freed, and Y. B. Band, J. Chem. Phys. **81**, 3091 (1984).

[49] T. A. Green and J. M. Peek, Phys. Rev. Lett. **21**, 1732 (1968).

[50] E. Charron, A. Giusti-Suzor, and F. H. Mies, Phys. Rev. A **49**, R641 (1994).

[51] Note that, in the calculations for the π states of the H($2l$) manifold in Ref. [22], there was a sign error in the matrix elements. This error did not affect qualitative behavior and led to only minor quantitative differences to the corrected calculations presented here.

[52] M. W. J. Bromley and B. D. Esry, Phys. Rev. A **69**, 053620 (2004).

[53] J. Colgan, M. S. Pindzola, and F. Robicheaux, Phys. Rev. A **68**, 063413 (2003).
[54] H. Mashiko, C. M. Nakamura, C. Li, E. Moon, H. Wang, J. Tackett, and Z. Chang, Appl. Phys. Lett. **90**, 161114 (2007).
[55] Z. Amitay, A. Baer, M. Dahan, J. Levin, Z. Vager, D. Zajfman, L. Knoll, M. Lange, D. Schwalm, R. Wester, A. Wolf, I. F. Schneider and A. Suzor-Weiner, Phys. Rev. A **60**, 3769 (1999).
[56] F. von Busch and G. Dunn, Phys. Rev. A **5**, 1726 (1993).
[57] P. Hansch, M. A. Walker, and L. D. Van Woerkom, Phys. Rev. A **54**, R2559 (1996).
[58] A. M. Sayler, P. Q. Wang, K. D. Carnes, and I. Ben-Itzhak, J. Phys. B **40**, 4367 (2007).
[59] A. Giusti-Suzor, F. H. Mies, L. F. DiMauro, E. Charron, and B. Yang, J. Phys. B **28**, 309 (1995).
[60] J. H. Posthumus and J. F. McCann, *Molecules and Clusters in Intense Laser Fields* (Cambridge Press, Cambridge, 2001).
[61] S. I. Chu and D. A. Telnov, Phys. Rep. **390**, 1 (2004).
[62] A. Giusti-Suzor, X. He, O. Atabek, and F. H. Mies, Phys. Rev. Lett. **64**, 515 (1990).
[63] G. Jolicard and O. Atabek, Phys. Rev. A **46**, 5845 (1992).
[64] J. H. Posthumus, J. Plumridge, M. K. Thomas, K. Codling, L. H. Frasinski, A. J. Langley, and P. F. Taday, J. Phys. B **31**, L553 (1998).
[65] J. H. Posthumus, J. Plumridge, L. J. Frasinski, K. Codling, E. J. Divall, A. J. Langley, and P. F. Taday, J. Phys. B **33**, L563 (2000).
[66] L. J. Frasinski, J. H. Posthumus, J. Plumridge, K. Codling, P. F. Taday, and A. J. Langley, Phys. Rev. Lett. **83**, 3625 (1999).
[67] B. Gaire, J. McKenna, F. Anis, M. Zohrabi, J. Hua, A. Sayler, N. G. Johnson, K. D. Carnes, B. D. Esry, and I. Ben-Itzhak (unpublished).
[68] G. N. Gibson, L. Fang, and B. Moser, Phys. Rev. A **74**, 041401(R) (2006).
[69] F. Anis, T. Cackowski, and B. D. Esry, J. Phys. B **42**, 091001 (2009).
[70] J. J. Hua and B. D. Esry, Phys. Rev. A **80**, 013413 (2009).
[71] J. J. Hua and B. D. Esry, Phys. Rev. A **78**, 055403 (2008).
[72] L. B. Madsen, Phys. Rev. A **79**, 043405 (2009).
[73] B. D. Esry, A. M. Sayler, P. Q. Wang, K. D. Carnes, and I. Ben-Itzhak, Phys. Rev. Lett. **97**, 013003 (2006).
[74] S. Saugout, E. Charron, and C. Cornaggia, Phys. Rev. A **77**, 023404 (2008).
[75] I. Ben-Itzhak, P. Q. Wang, A. M. Sayler, K. D. Carnes, M. Leonard, B. D. Esry, A. S. Alnaser, B. Ulrich, X. M. Tong, I. V. Litvinyuk, C. M. Maharjan, P. Ranitovic, T. Osipov, S. Ghimire, Z. Chang, and C. L. Cocke, Phys. Rev. A **78**, 063419 (2008).
[76] T. Zuo and A. D. Bandrauk, Phys. Rev. A **52**, R2511 (1995).
[77] M. Plummer and J. F. McCann, J. Phys. B **29**, 4625 (1996).
[78] L.-Y. Peng, D. Dundas, J. F. McCann, K. T. Taylor, and I. D.Williams, J. Phys. B **36**, L295 (2003).
[79] B. D. Esry and I. Ben-Itzhak, Phys. Rev. A **82**, 043409 (2010).
[80] C. Wunderlich, E. Kobler, H. Figger, and T. W. Hänsch, Phys. Rev. Lett. **78**, 2333 (1997).
[81] C. Wunderlich, H. Figger, and T. W. Hänsch, Phys. Rev. A **62**, 023401 (2000).